Single-Photon Detectors Modeling and Selection Criteria for High-Background LiDAR

Klaus Pasquinelli, Rudi Lussana, Simone Tisa, Federica Villa, *Member, IEEE*, and Franco Zappa, *Senior Member, IEEE*

***Abstract*—Vision systems capable of acquiring both two-dimensional and three-dimensional information through Light Detection And Ranging are assuming ever-increasing importance, being this market driven by the push from automotive companies to develop systems to be integrated in self-driving vehicles. Among others, candidate sensors for these systems are avalanche photodiodes, single-photon avalanche diodes, and silicon photomultipliers. Avalanche Photodiodes provide a good robustness to high background light at the cost of requiring an analog readout, instead Single-Photon Avalanche Diodes offer the possibility to implement digital readout and single-photon sensitivity, but are prone to saturation at extremely high background levels. We compare these three single- and multi-photon detector topologies, operated either in linear or digital regime, aiming at identifying the best suited detector to achieve the highest performance in Light Detection And Ranging applications at the lowest optical power active illumination and in presence of intense background (e.g. 100 klux). We present Matlab modelling and simulations and their experimental validation. Eventually, we propose a nomogram (referred to 100 m target distance) for identifying the most suited sensor topology across different operating areas and constraints, in order to achieve at least 70% success ratio.**

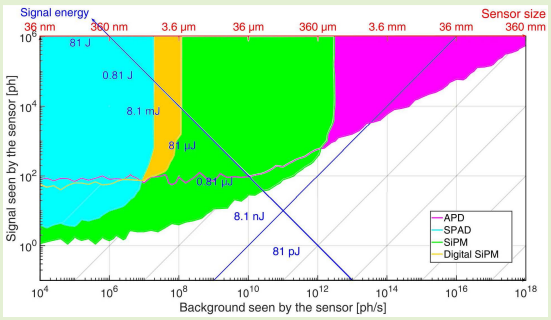

***Index Terms*—Single photon detectors, avalanche photodiode (APD), single-photon avalanche diode (SPAD), silicon photomultiplier (SiPM), 3D ranging, light detection and ranging (LiDAR).**

I. Introduction

DURING the last decade, many automotive companies, such as Waymo, Ford, Toyota, Tesla and others, have been investigating reliable autonomous driving vision systems. While some companies are investigating systems based on 77 GHz radar (mainly used for adaptive cruise control [1]) and pure two-dimensional (2D) vision [2], the great majority of the players are working on three-dimensional (3D) ranging systems, able to reconstruct obstacles' shape and position [3]. The most widespread approaches rely on Light Detection And Ranging (LiDAR), mostly based on shining a laser pulse towards the target scene and measuring the back-reflected light, in order to measure objects' distance either through actual "direct" (dTOF) or "indirect" (iTOF) Time-Of-Flight techniques [4]. The former is expected to achieve better signal-to-noise ratio with lower active illumination power, and can exploit various types of photodetectors and techniques, e.g. by raster-scanning a single detector through the overall field-of-view (FOV) [5], or with an array imaging the whole scene with no moving parts [6] [7]. Furthermore, Single-Photon Avalanche Diode [8] (SPAD) iTOF could measure wrong distances because different target colors, instead, dTOF systems are immune to this problem [9].

The automotive market requires extreme reliability and negligible failure-rate in all possible atmospheric conditions, with the lowest possible active illumination for achieving eye-safe, long-range (hundreds of meters) measurements. From this standpoint, SPADs are valid candidates since they can detect single photon [10]. However, their count-rate saturates to tens of million photons per second at most, that may be still lower than the worst-case condition for LiDAR, when strong background light reflects back from white, highly reflecting obstacles during the brightest day (up to about 100 klux). On the other hand, analog detectors can be easily operated in presence of high background light, but they

Manuscript received January 22, 2020; revised February 18, 2020; accepted February 24, 2020. Date of publication March 2, 2020; date of current version June 4, 2020. This work was supported by the EU's Horizon 2020 Research and Innovation Programme "Q-MIC" under Grant 801060. The associate editor coordinating the review of this article and approving it for publication was Prof. Bhaskar Choubey. *(Corresponding author: Klaus Pasquinelli.)*

Klaus Pasquinelli, Rudi Lussana, Federica Villa, and Franco Zappa are with the Dipartimento di Elettronica, Informazione e Bioingegneria, Politecnico di Milano, 20133 Milano, Italy (e-mail: klaus.pasquinelli@polimi.it; rudi.lussana@polimi.it; federica.villa@polimi.it; franco.zappa@polimi.it).

Simone Tisa is with Micro Photon Devices, 39100 Bolzano, Italy (e-mail: simone.tisa@micro-photon-devices.com).

Digital Object Identifier 10.1109/JSEN.2020.2977775

typically require higher optical power to overcome the intrinsic readout noise [11]. Avalanche Photodiodes (APDs) have internal gains, allowing for better sensitivity than other analog detectors, but they are still unable to match the single-photon sensitivity of SPADs, and also they require an analog readout circuit to interface the detector to the digital parts of the system. Eventually, Silicon-Photomultipliers (SiPMs) [12] extend dynamic range and provide multi-photon sensitivity and photon number resolution, through the parallelization of many SPADs with individual quenching resistors. Their ensemble response can be either analog or digital and can be used to develop pixels with multiphoton capability, but they must still avoid saturation and they still need an analog readout.

Other researches on this topic has been performed, for example on the time resolution of different photodetectors used in LiDAR applications [13]. In this paper, we compare these different single- and multi-photon detectors and techniques in order to identify which one requires the lowest laser optical power given the environmental conditions. In our analysis, we considered both analog and digital detectors, operated either in single-shot or repetitive accumulation mode, respectively, for exploiting their best performance in the most suitable operating condition. To this aim, we will present both plots of analog waveforms and time-resolved histogram distributions of detected events for the different detectors.

In our simulations we considered an automotive scenario, using 100 m as the maximum target distance and 3 ns (thus ~50 cm) as the discrimination time window of the acquisition system; this kind of analysis can be used to evaluate "long range" systems where a 50 cm error may be considered reasonable. This kind of system is not suitable for short range LiDAR, as parking system or similar where it is important to discriminate distances around 5 cm. To this aim, at first the three sensor topologies will be modelled and simulated in Matlab in Section II; then Section III will illustrate the optical system and electronic hardware for the measurements; Section IV will validate simulations with experimental results; eventually, Section V will derive a nomogram and will discuss different case-studies for SPADs (Section V.A), analog SiPMs (V.B), and digital SiPMs (V.C). Finally, Section VI will draw conclusions and perspectives.

The conclusions will be based on ideal photodetectors because different photodetectors have different constraints as noise, dark counts, efficiency and other various physical constraints such as, for example, the minimum SPAD size. Once all photodetectors are compared on a single nomogram, the user can evaluate if the device is suitable or not for a certain working point. In case it is not feasible, the user can adjust the axis of the nomogram (thus keeping the same shape of the working region) in order to have an idea if such a device can become suitable. This point will be clarified in the Conclusions.

II. Simulations

In order to compare single-photon and multi-photon detectors in different operating conditions, we developed Matlab scripts, which take as inputs the main system-level parameters (e.g., object distance, reflectivity, detection rates due to ambient background and active illumination, and optical efficiency) and output the time-domain waveform response.

The solar background photon rate is computed [14] as:

$$C_{pixel,sun}(\lambda) = E(\lambda)\cdot\cos\theta\cdot\rho\cdot A\cdot\left(\frac{1}{2F\#}\right)^2\cdot\frac{1}{N_{pixel}}\cdot t_{bin} \quad (1)$$

where λ is the active illumination wavelength, E is the number of background photons per second per square meter [15], θ is the angle between the normal of the target surface and background source, ρ is the target reflectivity, A is the detector sensitive area, F# is the f-number of the optical system, N_{pixel} is the number of the pixels (in case of a detector array), and t_{bin} is the simulation time-step. Instead, the signal photon rate [14] is given by:

$$C_{pixel}(z) = P_T\cdot\frac{\lambda}{hc}\cdot\rho\cdot\left(\frac{D}{2z}\right)^2\cdot\frac{1}{N_{pixel}}\cdot t_{bin} \quad (2)$$

where P_T is the emitted power, D is the aperture, and z is the target distance from the objective. In addition, the scripts include detector-specific parameters. For APDs: gain, bandwidth, quantum efficiency (QE), dark current, and excess-noise factor (ECF). For SPADs: pixel fill-factor (FF), PDE, dead-time, dark count rate, and time-jitter. For SiPMs: gain, number of cells, recovery time, time-jitter, photon-detection efficiency (PDE), dark count rate, and single-photon output waveform, with a Gaussian peak and an exponential decay [21].

Each simulation begins with the creation of a numerical vector containing the average number of background photons in each 10 ps time-bin and the signal photons across the bins corresponding to the given Time-Of-Flight (TOF), i.e. to the target distance, spread as a Gaussian distribution around the expected TOF, following the Poisson statistics [16]. Then, the numerical vectors are processed as detailed in the following sections, depending on the detector-specific parameters. Eventually, the simulated TOF return peak is identified and its time-position is compared to the expected TOF, with a 3 ns tolerance window. Such large window is needed to compensate the left time shift of the received signal due to the increasing power of the light source, so it is possible to use the same window position for all measurements. If the signal power is increased, the power of the signal tail will also increase, so it happens that photons in the tail overcome the background light and saturate the sensor before the signal reaches the maximum amplitude causing a left shift of the detected peak. The simulated measurement is considered successful if the identified peak falls within the tolerance window and wrong otherwise. This evaluation is repeated 20 times for each background and signal combination to evaluate the "success ratio", i.e. the percentage of measurements fallen inside the tolerance window, in order to estimate the measurement reliability.

The outcomes of such quantitative comparisons will be analyzed in Section V, where a general-purpose nomogram will also be presented. 20 repetitions for each point will give us a 5% quantization in the results. In paragraph IV, Figure 18 shows that a quantization of 5% is sufficient to our purpose: the "noise" on the success ratio is very low. Taking into consideration where the APD does not operate properly, the error rate is $< 5\%$. For this reason, there is no

significant advantage in further increasing the quantization (i.e. the number of repetitions).

A. APD, Avalanche Photodiode

In order to analyze the APD response, the average number of photons in the numerical vector is amplified by the overall (APD and front-end circuit) gain, with the addition of noise contributions (namely electronic noise, Poisson variance, and excess noise).

Given the APD analog response, a single laser pulse (containing many photons) may be recorded one-shot, with no need for repetitive laser excitations. The resulting vector is then low-pass filtered, taking into consideration both APD and electronics bandwidths, and eventually converted into the corresponding voltage waveform, through the transimpedance amplifier of the front-end electronics with an overall noise of about 6 mV_{RMS}.

The excess noise factor has been evaluated comparing the simulations with acquisitions made by using a known DC light source: the obtained value has been 13.

In order to avoid amplifier saturation, a 1.6 kHz high-pass filtering is applied to suppress the strong DC background, which translates into a constant output voltage baseline. Figure 1 shows a simulated output waveform for an APD.

B. SPAD, Single Photon Avalanche Diode

Differently from the APDs, to make an estimation of the target distance using SPADs, repeated measurements are required in order to realize histograms with the photons' arrival time. Being capable to see only one photon per frame it is not possible to work single shot with SPADs.

Moreover, SPADs are inherently digital, thus with no noise contribution due to readout and excess factor. However, they require a dead-time after each ignition, to properly quench the avalanche process and recover completely the PDE, limit afterpulsing [17], and reset the detector back to operation. Dead-time lasts about tens of nanoseconds for Silicon SPADs and even some microseconds for InGaAs/InP ones, suitable for near-infrared applications up to 1.6 μm wavelength [18]. Such dead-time causes signal distortion, because the SPAD is blind therein; hence the measured signal detection rate decreases and a constant background light results in an exponential decaying distribution of detected events (see Figure 2) because early photons have higher probability to be detected compared to late ones. This effect is also known as "pile-up" distortion [19].

In the followings, we consider the SPAD capable to detect only one photon per laser shot, i.e. with a dead-time longer than the interval between two laser pulses or with a timing electronics (e.g. a Time-to-Digital Converter, TDC) able to perform and store only one TOF conversion per laser pulse. This is indeed the case when a single SPAD (with a single TDC) is scanned across the scene under observation and also when an array of SPAD pixels (each with a SPAD and a TDC) is employed as a 3D ranging imager with no need for scanning.

The simplest approach for the peak detection is to identify the histogram bin with the highest number of simulated detections; however, the pile-up distortion could cause errors (see for example the first 40 ns of the blue histogram trace in Figure 2). Thus, first we fit the histogram with an exponentially decaying curve (red trace in Figure 2), which is then subtracted from the original histogram, in order to get rid of most of the background photons (Figure 3), and eventually we identify the highest peak (corresponding to 190 ns in this example, i.e. to a distance of 28.5 m).

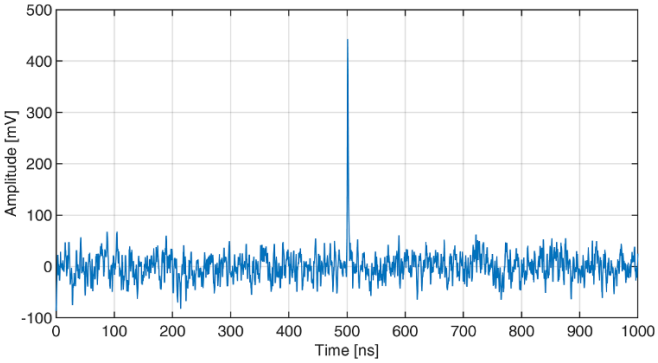

Fig. 1. Simulated time-domain waveform of the APD detector for a 500 ns TOF measurement.

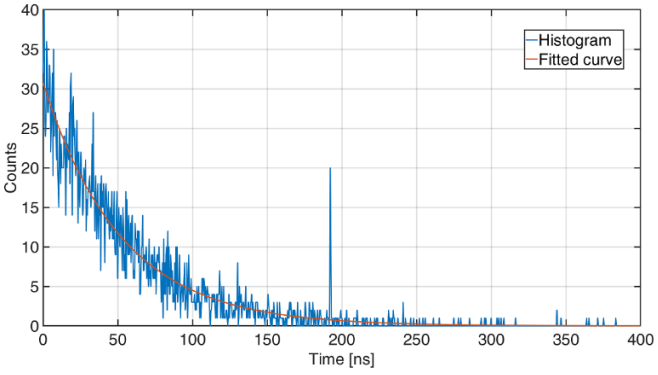

Fig. 2. Simulated TOF histogram (blue) of a 30 μm diameter SPAD and its fitted curve (orange) across a 400 ns frame-time.

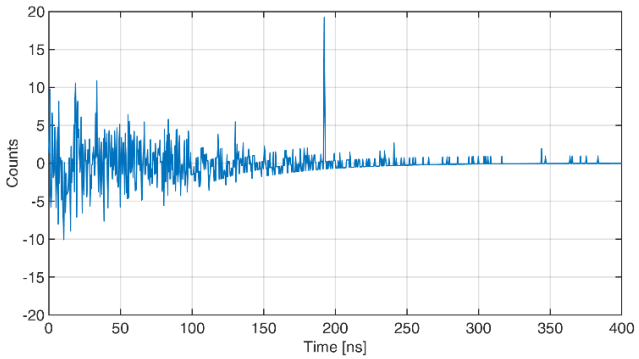

Fig. 3. Result of the subtraction of the fitted exponential decay from the histogram in Figure 2, in order to detect the TOF peak.

C. Analog SiPM, Silicon PhotoMultiplier

An analog SiPM consists of many microcells made by one SPAD and one quenching resistor each, connected in parallel

to provide an output current pulse proportional to the number of detected photons. Given the analog nature of the microcell's passive quenching circuit, it is important to correctly model the recovery transition of each microcell.

In fact, the SPAD excess bias V_{EX} (voltage difference between the applied voltage and the breakdown one) drops to zero (self-quenching) almost suddenly after each avalanche triggering and then it recovers to the quiescence value (reset transition), with an exponential time constant given by the quenching resistance and the SPAD stray capacitance. The PDE dependence on V_{EX} can be approximated as [20]:

$$PDE\,(t) = QE \cdot \left[1 - e^{-\frac{V_{EX}(t)}{V_C}}\right] \tag{3}$$

where QE is the quantum efficiency of the SPAD, dependent on the wavelength of interest and on the junction depleted width, and V_C is a fitting parameter. For modelling the detection probability, the vector containing the randomized photons is scanned and every time a photon is encountered, an actual detection is marked only if a randomly generated number is lower than the probability:

$$P_{tot}(t) = 1 - [1 - PDE(t)]^{N_{ph}} \tag{4}$$

where N_{ph} is the number of photons in the bin. Note that P_{tot} is also time dependent, because *PDE*depends on V_{EX} and that to use P_{tot} it must be scaled by the FF. In case of success, the photoelectron response is saved in a new vector, with a time-dependent photo-electron time-dependent gain given by:

$$G\,(t) = G_0 \cdot \left(1 - e^{-\frac{t}{\tau}}\right) \tag{5}$$

where τ is the microcell's time recharge constant and G_0 is the maximum gain given by the SiPM producer.

In the SiPM the time dependence of the gain has to be added in simulations because the gain drop is much more evident, because after each event there is a complete discharge of the SiPM capacitance. Once all events of all microcells are accumulated into a final vector, the resulting waveform is convolved with the exponential decay and the capacitive coupling given by the capacitor in parallel to the quenching resistor which provide a fast peak before the exponential decay [21] (the various components of the simulation can be seen in Figure 4). Finally, the photocurrent is converted into a voltage waveform and filtered (similarly to the APD case, in Section II.A), through the transimpedance of the external amplifying stage. Figure 5 shows a result example. Differently from the APD, in this case not only the electronics can reach the saturation but also the SiPM itself can saturate, having it a finite number of cells, it saturates when all the cells are triggered.

We crosschecked our Matlab simulations with electrical circuit simulations of actual SiPMs, based on the SPICE model reported in Ref. [21]. Figure 6 shows the excellent matching when a SiPM with just 10 microcells is considered in order to highlight the quantization of peak intensities and decay time constants. Note that, for the synchronicity between the Matlab (randomly) simulated triggering events and those simulated in SPICE, we employed the generated photon sequence in Matlab to trigger the microcells' SPICE models.

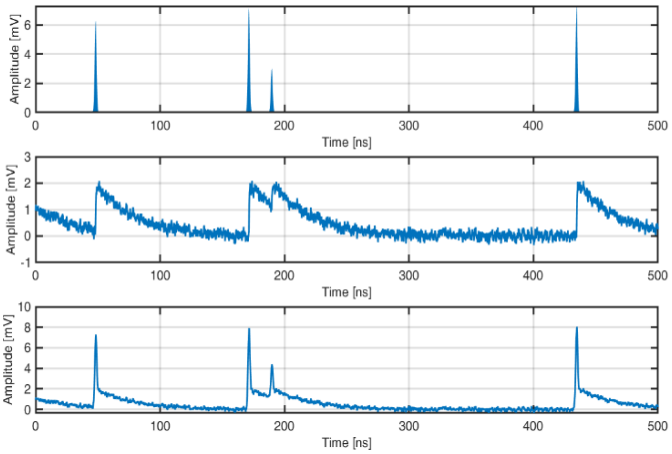

Fig. 4. Simulation steps for an analog SiPM: capacitive coupling (top), exponential decay (center), sum of the two components (bottom).

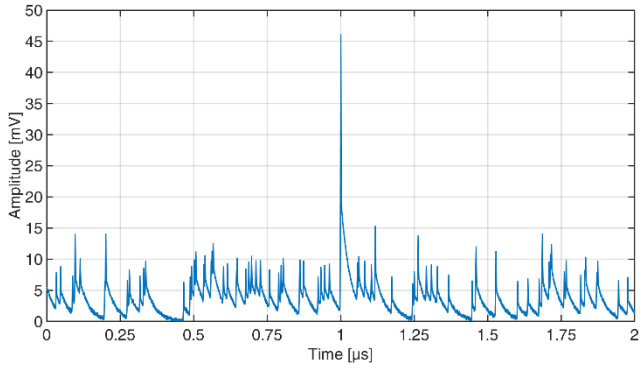

Fig. 5. Simulated analog SiPM response, where every decay is a one-microcell event (due to either a background photon or a dark event) whereas the peak at 1 μs is due to the laser shot's simultaneous photons.

D. Digital SiPM

The actual limitation in measuring the TOF of each photon detected by a SPAD (as in the simulations of Paragraph II.B) is often the maximum throughput of the Time-to-Digital Converter (TDC) electronics, since the TDC conversion time is usually longer than the SPAD dead-time. For this reason, hybrid topologies with arrays of SPADs and shared TDCs have been proposed in literature, in which the TDC gets triggered only when a proper number of photons are detected at the same time in a sub-array. For example, in Ref. [22] the four SPADs of a microcell share one TDC, which gets triggered when a predefined number of SPADs get triggered (e.g. two SPADs), thus reducing unwelcome events related to background photons (usually random in time and not concurrent).

As digital SiPM, we consider an array of independent SPADs with own active quenching circuitry, able to trigger one single TDC. Therefore, the digital SiPM cannot provide a 3D ranging image of the full scene, but it acts as a single point detector. Instead, an array of x $\times$ y digital SiPMs with one TDC each (i.e. x $\times$ y TDCs in total), could provide 3D ranging maps.

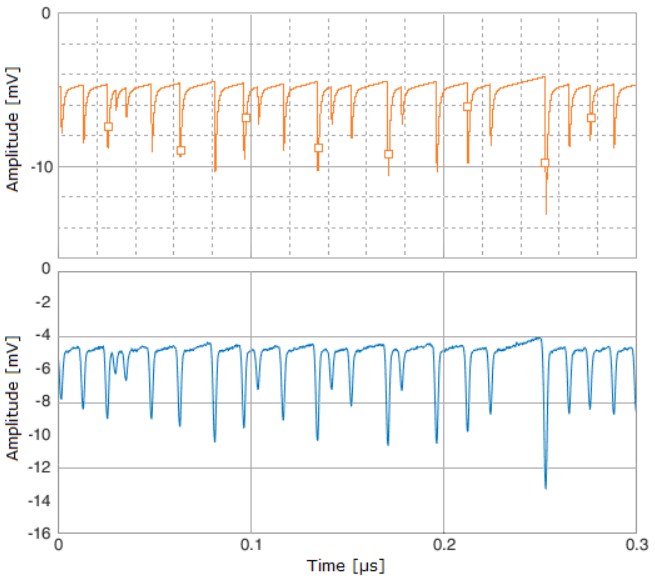

Fig. 6. Comparison between SPICE (top) and Matlab (bottom) simulations of an analog SiPM behavior. Note that the output has negative values because the SiPM was simulated for an anode-readout.

In order to simulate the digital SiPM, we used the same algorithm of Paragraph II.B but, instead of disabling the SPAD for the whole remaining frame time after each triggering, we implemented a fixed dead-time duration (20 ns i.e. shorter than the frame period) after each ignition in each SPAD, after which the PDE is completely restored [23]. As an example, for a digital SiPM with 3 × 3 SPADs with threshold set to 2 coincident photons, we start from 9 numerical vectors containing the incoming photons for the 9 SPADs, then we scan all them with a coincidence time-window (e.g., 2 ns wide) and we generate a TDC triggering event as soon as at least two photons are found within the time-window. An example of comparison can be seen in Figure 7. In a "standard" SPAD camera, the SPAD can see only one photon per frame. Instead, the possibility to see more than one photon per frame enable the pixel to see coincidences also if all SPADs have been triggered previously by background photons. Since the TDC dead-time is much longer than the SPAD quenching dead-time, we have to reduce the number of triggering events in order to start conversion only when it is more probable that the event is related to signal and not to background, so the TDC is being triggered only one time per frame when a coincidence event occurs. This can be a solution to reduce the TDC conversions due to background and, theoretically, to increase the number of conversions related to the signal.

III. Measurements Setup

For validating modelling and simulations, we developed the optical setup shown in Figure 8, capable of testing two photodetectors at the same time, while imaging the same scene at exactly the same conditions (i.e. signal and background photon rates). A 25 mm focal length objective focuses the incoming light onto a diaphragm, which allows to adjust FOV and desired signal-to-noise ratio. In fact, since the return

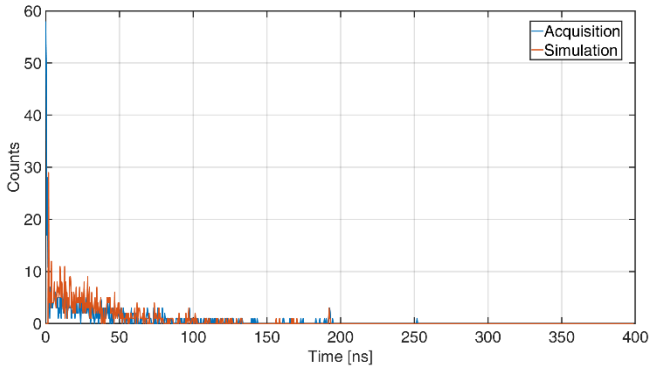

Fig. 7. Example of an acquisition and a simulation of a digital SiPM. The dSiPM acquisition is realized using post-processing and SPAD camera capable to see only one photon per frame for each pixel (no rearm after the first photon). To evaluate the coincidences, we used the TDC data of the 4 SPADs present in a generic 2 × 2 subarray.

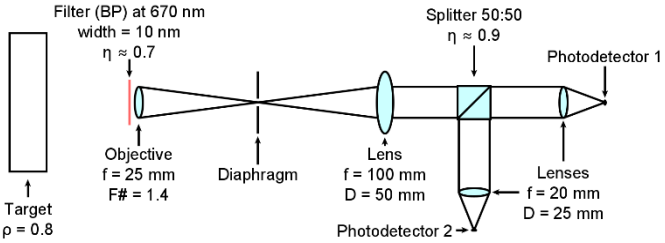

Fig. 8. Optical system to compare the behavior of two different photodetectors at the same time, including target object, objective with bandpass filter, diaphragm, collimating lens, beam splitter and focusing lenses.

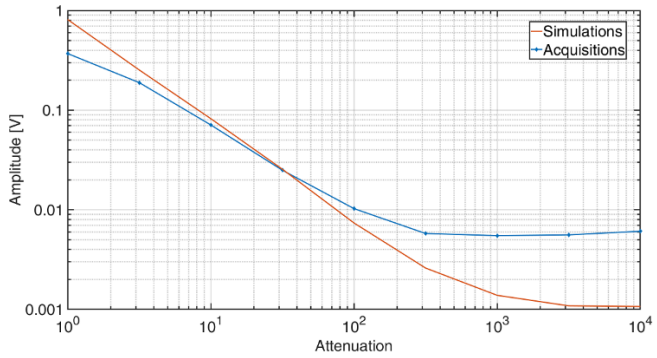

Fig. 9. Measurements and simulations of APD signal peak amplitude versus optical attenuation (using neutral density filter). At the maximum signal (with no attenuation), about 3300 signal photons per pulse on average reached the detector.

laser spot covers an area much narrower than the FOV, the diaphragm affects just background and not the laser signal.

A 10 nm bandpass (BP) filter centered on the laser 670 nm wavelength is placed in front of the objective to reduce the background light. The rays are then collimated by means of a converging lens with 100 mm focal length and 50 mm diameter and split onto the two photodetectors by means of a 50:50 beam-splitter, through two twin converging lenses with 20 mm focal length and 25 mm aperture. For the overall system, we computed a 63% overall transmittance efficiency at 670 nm wavelength.

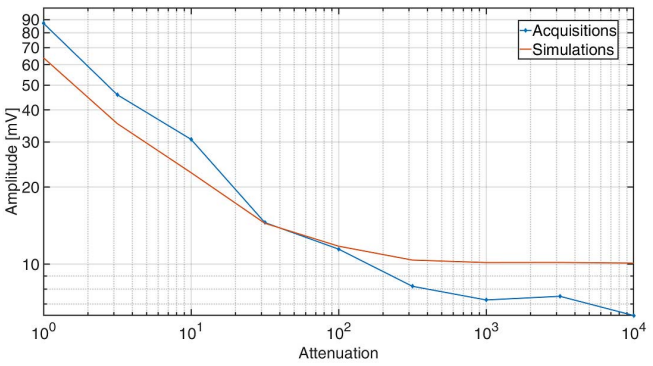

Fig. 10. Measurements and simulations of APD background RMS noise versus optical attenuation (using neutral density filter), with a $6{\cdot}10^{18}$ ph/(s·nm·m^2) background illumination.

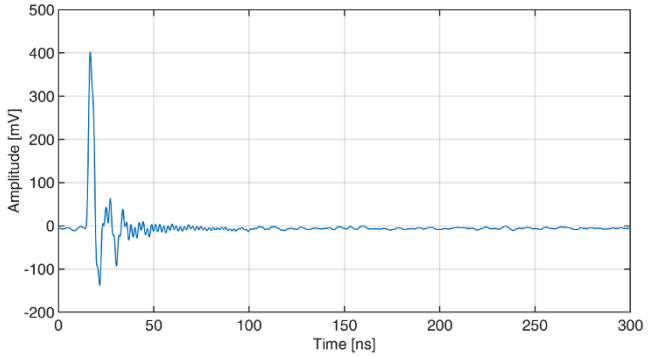

Fig. 11. Measured waveform at the transimpedance amplifier output for the APD detector. Note the undershoots due to residual ringing.

We employed a 670 nm laser with 400 ps Full-Width at Half Maximum (FWHM) and 200 mW peak power. The used repetition rates of the laser were variable from 10 kHz to 1 MHz using always periods much longer than the detectors transients. As background light we employed either natural solar illumination (during favorable day-light conditions) or an LED and halogen lamp, whose power was adjusted in order to match solar illumination.

Concerning detector readouts, both APDs and analog SiPMs were coupled to a 450 MHz bandwidth Transimpedance Amplifier (TIA) and the output voltage waveforms were acquired by means of a 1 GHz bandwidth oscilloscope. Instead, SPADs were connected to on-chip quenching circuits [9], whereas a SPAD camera [3] was exploited to emulate the digital SiPMs by identifying concurrent detections from a pixel subset.

IV. Measurements and Results

We validated the APD modelling by comparing the signal amplitude of measurements and simulations (Figure 9) and the root mean square (RMS) values of both background and electronic noises (Figure 10).

We attenuated the laser beam and the background through neutral density filters, while background power density and laser peak power were fed to the simulator as parameters. We employed an APD produced by Excelitas (C30737LH-500-80A-ND [24]), with 135 V bias and 500 μm diameter.

The differences at low attenuations in Figure 9 and Figure 10 are due to electronics partial saturation, whereas small oscillation and ringing limit the minimum detectable signal, thus causing an error for high attenuation values, as can be seen in Figure 11.

We validated the SPAD modelling by comparing measured and simulated background- and signal-photon rates, for a given number (1000) of laser-pulse repetitions. Figure 12 shows the good matching: the detection rate decrease over time is caused by background photons pile-up, as described in Paragraph II.B.

We validated analog SiPM simulations and measurements when employing a HAMAMATSU S13360-1350CS SiPM (with 667 microcells, and 1.3 mm^2 total active area) TIA with a 240 Ω transimpedance, by comparing the output

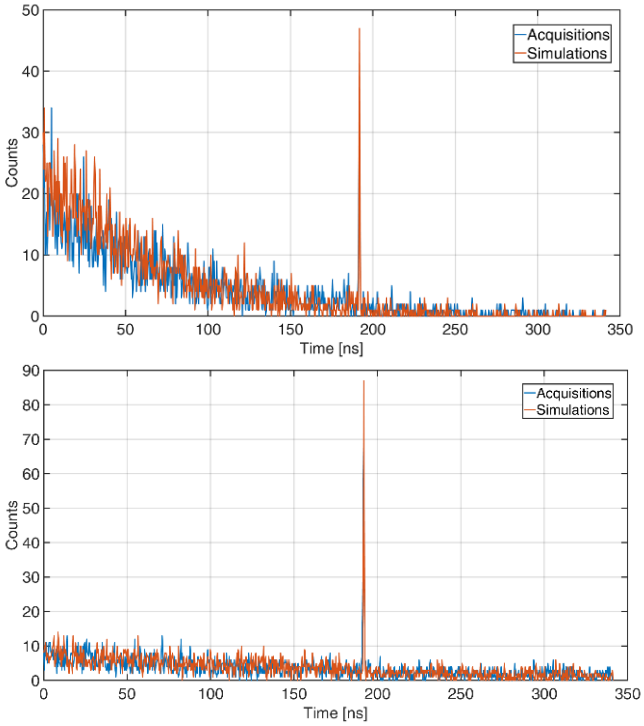

Fig. 12. Measurements and simulations of SPAD time-of-flight histograms, with no (top) and $10^{0.5}$ (bottom) attenuation of background and laser signal. At no attenuation, about $3{\cdot}10^{17}$ ph/(s·nm·m^2) background photons and 3300 signal photons per pulse reached the detector on average.

voltage standard deviation of background signal, the laser peak intensity, and the mean output value due to the background (since no high-pass filter was used, on purpose). Thanks to the extremely high ($1.7{\cdot}10^6$) intrinsic gain of the SiPM, the measured dynamic range spans from a single-photon up to about 500 concurrent photons.

We fitted the simulation of the single photon response shown in Figure 13, where the exponential decay due to time constant and the peaked capacitive coupling [21] is clearly visible. We also verified the gain of the tested device with respect to the nominal value of the gain in the HAMAMATSU S13360-1350CS datasheet [25].

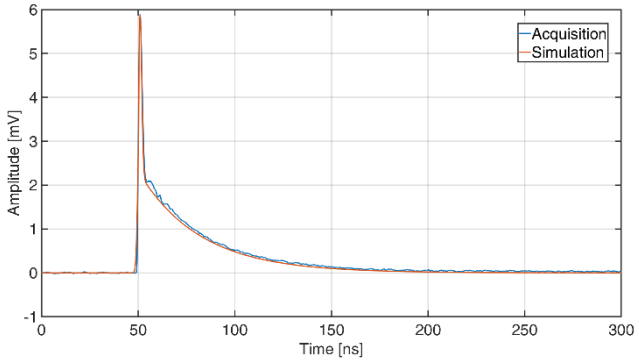

Fig. 13. Measured and simulated waveforms of the single-photon pulse response of one SiPM under test, with the typical peaked capacitive coupling (at 50 ns) and the exponential decay (about 40 ns time constant).

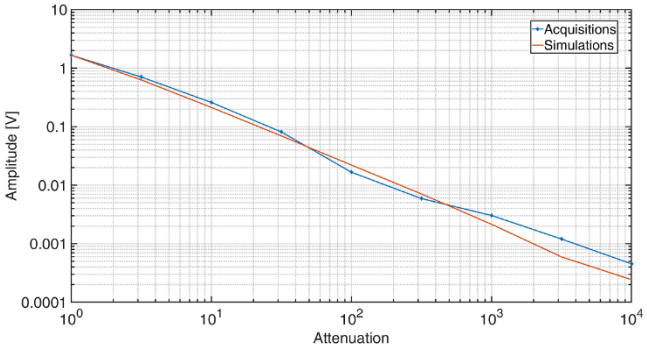

Fig. 14. Measurements and simulations of the analog SiPM laser peak amplitude versus signal attenuation, in dark conditions. At no attenuation, about 3300 signal photons reached the detector.

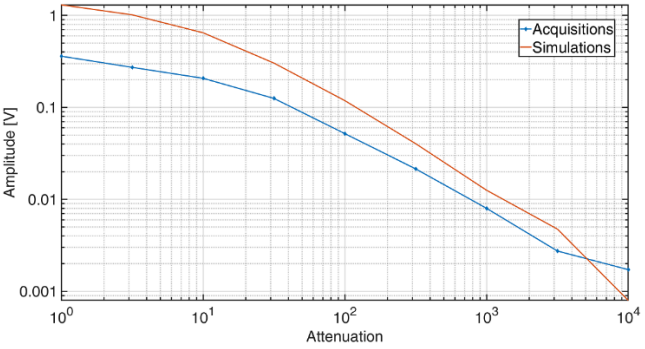

Fig. 15. Measurements and simulations of the analog SiPM average background level versus attenuation, with a 10^{18} ph/(s·nm·m^2) background, corresponding to 22.5 klux.

Figure 14 shows the good matching between simulations and measurements of the analog SiPM's laser peak response. For maximizing the detected signal, the SiPM was slightly defocused, in order to spread the light spot across many microcells. Then, in order to avoid SiPM self-heating, the laser repetition rate was lowered to tens of kHz, instead of 2.5 MHz as employed for the measurements of all other detectors.

Figure 15 shows the SiPM average background level: the mismatch between simulations and measurements is due to thermal drift caused by self-heating. In fact, each degree of

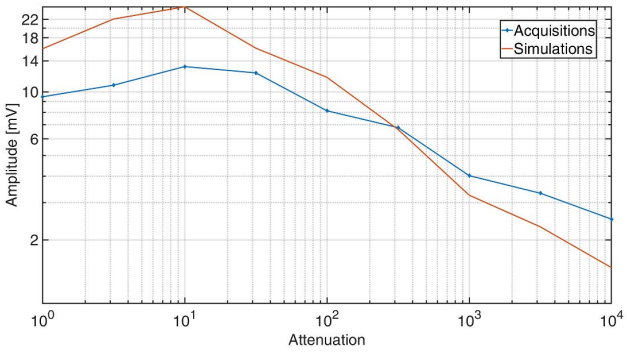

Fig. 16. Measurements and simulations of the analog SiPM RMS noise versus attenuation, with a 10^{18} ph/(s·nm·m^2) background, corresponding to 22.5 klux.

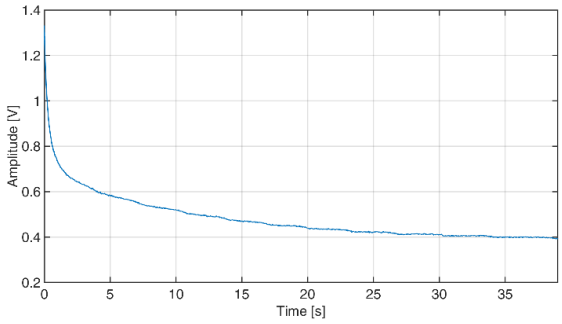

Fig. 17. Thermal drift of the TIA's output voltage baseline (i.e. the SiPM average photocurrent) due to self-heating of the detector, with constant 10^{18} ph/(s·nm·m^2) background.

temperature causes the breakdown to increase by 54 mV; with high background (and consequently high-power dissipation from the device), we estimated a loss of excess voltage of about 1.5 V ÷ 2 V (30 °C ÷ 40 °C above the ambient temperature).

Since the die temperature could not be directly measured, we also evaluated the gain loss by observing the single photon amplitude versus temperature using a climate chamber to heat the SiPM. The same considerations apply to the comparison of RMS noise shown in Figure 16.

In order to further investigate the self-heating issue, we measured the drift of the average TIA's output voltage baseline, with constant background, starting a dark acquisition with the SiPM at room temperature. As shown in Figure 17, a background of 10^{18} ph/(s·nm·m^2), corresponding to 22.5 klux, causes a decrease in the output baseline from 1.3 V down to 400 mV in about half a minute: this trend quantitatively explains the gain loss experienced in Figure 15 and Figure 16.

In order to check performance of a digital SiPM approach, we employed a SPAD camera, set to provide only one single photon detection per SPAD and per frame (i.e., per laser pulse). For each frame, we selected an n × n array sub-set and we checked the photons arrival time to find time-coincidence of m concurrent photons (with m included between 2 to 5). Then we repeated the acquisition in order to build a histogram of coincident arrival-times, with various threshold, m, and matrix size, n, to evaluate performance trends.

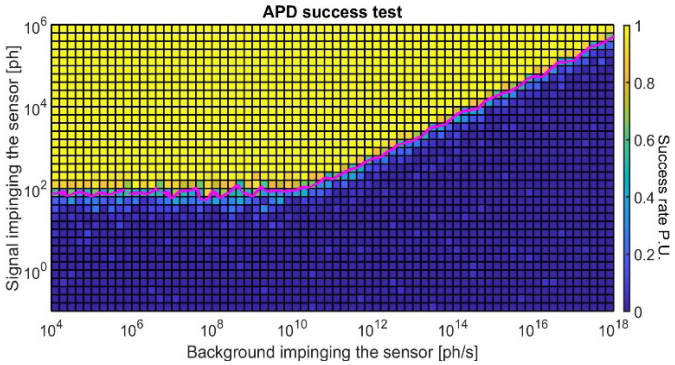

Fig. 18. Color plot of an APD. The X axis is the background photon rate impinging on the sensor, the Y axis is the number of signal photons imping on the sensor. The color or each cell represent the success rate per unit (P.U.) according to the color bar on the right. The magenta line represents a success rate of 70%: the horizontal region at low background is dominated by the intrinsic noise of electronics and APD, while the oblique component is due to the light Poissonian noise.

Unfortunately, the employed SPAD camera, being able to detect only one photon per SPAD per frame, cannot provide the full benefits of a custom digital SiPM device, which could detect more than one photon per frame. Moreover, by employing only few TDCs that are triggered only when m concurrent photons are detected can give a great improvement in terms of chip complexity, power dissipation, and data throughput. In fact, SPADs can be quenched and reset (after a dead-time), so to be reused within the same frame to see other photons, increasing in this way, the possibility to detect multi-photon coincidences.

Table I summarizes the photodetectors' parameters and the used algorithms.

V. Operating Areas and Nomogram

Once we validated the good matching between Matlab simulations and experimental acquisitions (as shown in the previous paragraph, where simulations and acquisitions were compared by checking RMS noise values and signal peak values), we were able to predict the outputs from each detector even outside the limits set by the experimental setup, including laser and background sources. The behavior outside the setup limits will be fair because it consists of adding only more signal and background photons: increasing photons will increase events according to statistics behavior and physics models.

The only difference with a real model is that the simulations have no electrical saturation that however is good because the saturation is different from system to system because it depends on how it is designed. In a real LiDAR system, we must evaluate case by case if the electronic saturation is reached, this is strongly dependent on used components and design choices. The intrinsic noise of the detectors can be neglected because, in high background applications the light's "Poisson noise" is the main component. So, the nomogram that will be presented in this paragraph can be used as an estimation of the working point of a selected photodetector. We simulated APDs, SPADs and SiPMs across a wide operating range, from 0.1 up to 10^6 returning signal photons and from 10^{10} ph/(s·nm·m^2) (a very weak lamp) to 10^{20} ph/(s·nm·m^2) (more than a summer full sunny day) background. Note that single-shot measurements were considered for APDs and analog SiPMs multi-photon detectors; instead 1000-repetitions (with the same total energy of the single shot) were considered for SPAD and digital SiPM single-photon detectors, in order to build the TOF histogram.

TABLE I
Summary of the Photodetectors (APD [24], SPAD [9], SiPM [25]) Specifications, Parameters and Algorithm Used for the Simulations

	APD	SPAD	SiPM	dSiPM
Bias	135 V	30 V	55 V	30 V
Detector gain	90	Digital output	$1.7{\cdot}10^6$	Digital output
External amplification	TIA	×	TIA	×
Number of cells	1	1	667	2 × 2 and 3 × 3
Algorithm	Peak finder in single shot	Peak finder in histogram	Peak finder in single shot	Peak finder in histogram

Being interested in LiDAR ranging applications, we considered successful a test where a peak finder algorithm identified the laser peak in the detector's response waveform (i.e. the TOF echo) within a 3 ns acceptance-window compared to the set distance. In a real application, the peak finder algorithm can be improved with a variable threshold algorithm, dependent on the background mean value, this could reduce the system timing performance (though with a 3 ns window, that could be negligible). We computed the success ratio for each detector typology and for each combination of background and signal intensities over 20 simulation runs. Then, we plotted these values in a two-dimensional color plot, like the one in Figure 18 (made for a normalized APD with 100% QE).

However, detectors may have different size and fill factor: in particular, our test setup comprised a 500 μm diameter APDs, 30 μm diameter SPADs and a square SiPM with 1.3 mm side. Therefore, each detector has different FOVs, preventing the 2D color maps from providing a fair comparison among the detectors (as the same background causes higher photon flux in larger detectors). Also fill factor causes a similar issue, since it attenuates both signal and background. Furthermore, the number of microcells in a SiPM affects its dynamic range and consequently its capability to be used with higher background.

Eventually, for a fair comparison, we generated 2D maps based on the photon rate over a normalized area and a 100% fill factor, considering a 667-microcell SiPM (as for the Hamamatsu device we tested), and a 3 × 3 sub-array size for the digital SiPM with a coincidence threshold of 2 photons. Figure 19 shows the normalized nomogram in these conditions: the colored border lines are the boundaries where the "success ratio" of the correct TOF acquisition is 70%. Higher success is met moving toward upper- and left-most working regions, i.e. at higher signal and lower background levels; instead, lower-right regions represent conditions where the detector is unable to measure the target distance with

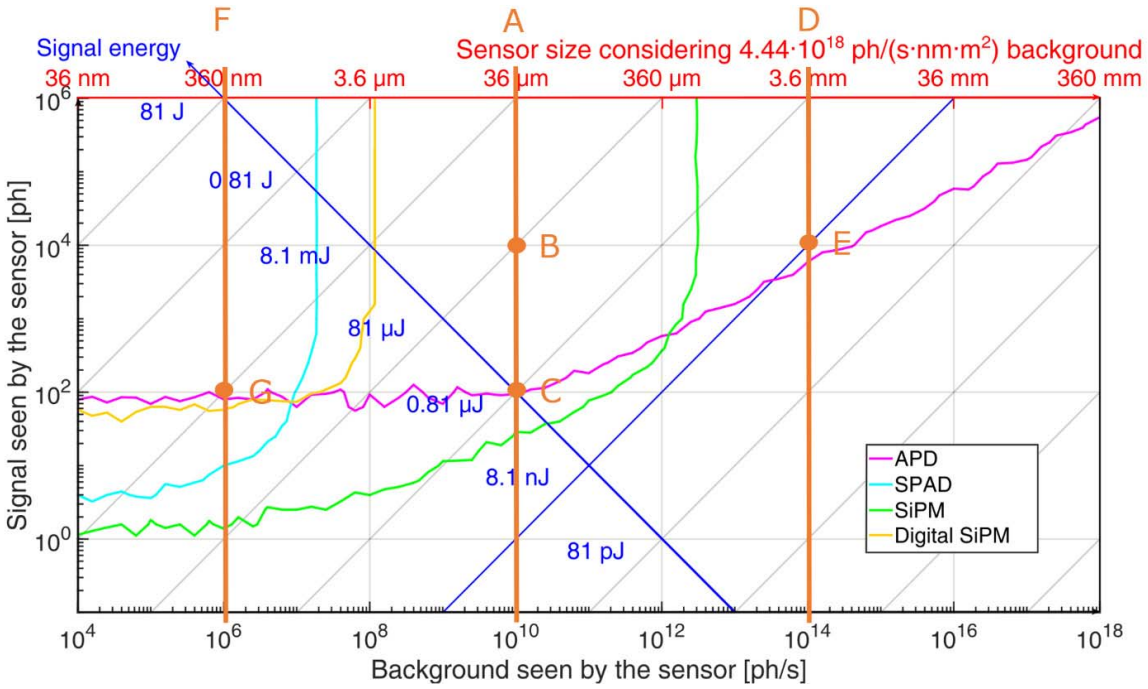

Fig. 19. Ideal detectors' nomogram, as a function of impinging background photon rate (horizontal bottom axis), number of impinging signal photons (vertical left axis), sensor size (top horizontal red axis), and signal energy (slanted blue axis). The border lines are those where the "success ratio" is 70%; higher success is met in the upper- left-most area of the working regions (i.e., for higher signal and lower background levels). The vertical lines and marked working points are discussed in the text.

adequate reliability. As can be seen, the SiPM is able to reach the required reliability with fewer photons and higher background than the single-pixel SPAD. The worse SPAD performance is due to the required repetition of measurements (1000 considered so far), which causes a 1000× increase in background (both ambient light and dark counts). The APD can work at higher background levels but needs more signal photons to properly detect a peak, even with no background, because of the electronics readout noise. Finally, the digital SiPM provides slightly better performance than the single SPAD at high backgrounds (see Paragraph V.C).

Referring back to Eq. 1, it is important to highlight that, once the optical parameters are fixed, the only free parameter is the choice of detector size. For instance, in our simulation we chose an F/1.7 optical system, ±1° FOV, 20 nm width filter and 100% target reflectivity. Having fixed these parameters, and considered a fixed $4.44{\cdot}10^{18}$ ph/(s·nm·m^2) (i.e. 100 klux at 670 nm) ambient light illuminating the 100% reflective scene, the background photon rate is only proportional to the detector active area: therefore, we can replace the horizontal axis in Figure 19 with a new axis for the detector side size (red axis). For instance, a 10^{10} ph/s background on the detector corresponds to a 36 μm side detector, as shown with the "A" orange line.

The nomogram can also be used to estimate the laser power required to achieve a desired success ratio (i.e. measurement reliability), at a given sensor size and target distance. Since an increased distance only affects the number of returning signal photons and not the background (as long as the background light is uniform across the whole scene), this corresponds to a down-right shift of the blue 45°-slanted axis. The nomogram in Figure 19 considers a fixed 100 m distance, for autonomous driving scenarios. The axis is tilted by 45° because, for a given number of emitted photons, the detector collects more photons when the sensor size is increased (see Eq. 2). Hence, if detector size is increased by a decade, the detector collects 100× more photons, if other parameters stay unchanged.

For example, with the aforementioned optical system, a 36 μm square detector, with $4.44{\cdot}10^{18}$ ph/(s·nm·m^2) background, 20 nm filter width, 100% target reflectance at a distance of 100 m operates along line "A". Therein, we can choose a SiPM with 667 cells or an APD, while other detectors (SPAD and digital SiPM) are not able to operate under these conditions. If we may use an 81 μJ laser pulse, both SiPM and APD would be suitable sensors (see point "B"), whereas with a laser energy reduced to 0.81 μJ the APD becomes borderline (point "C"). Note, though, that a 24 μm side SiPM with 667 microcells therein is unrealistic (see paragraph V.B).

This has been used because we used a 667 cells SiPM to compute the model. We also performed other simulations with 4, 16, 64, 256, 1024 cells to provide the trend of the improvement with the increasing number of cells: the results will be shown in paragraph V.B. It is clear that is impossible to have a SiPM of 24 μm side, with 667 cells, but maybe it can become an actual SiPM if efficiency and FF are lower: for example a 1 μm^2 SiPM with a 100% FF will be similar to a 60% FF 1.67 μm^2 SiPM; to recover the loss of efficiency and/or FF a larger photodetector is needed. A possible way to reduce the required illumination power is to increase sensor size, for example to 2.4 mm (line "D"): however, only the APD could reach a 70% success ratio (with at least 8.1 nJ

laser pulse energy, point "E"), whereas others fail because of the very high background detection rate.

Instead, in order to employ SPADs and possibly in dense arrays, it is necessary to reduce the sensor size (line "F"), as this allows to effectively attenuate ambient background. However, this also causes signal attenuation, thus forcing to increase laser energy to 8.1 mJ (point "G"): with the same background a smaller sensor collects fewer background photons, but also fewer signal photons; therefore, the laser energy must be increased in order to collect a proper number of signal photons.

These numbers can be rescaled for operation at distances different than 100 m: for instance, in case of short-range operation within 10 m, the required energy is reduced by a factor 100, thus reducing to 81 μJ pulse energy for point "G".

Since real systems feature an overall efficiency lower than 100% and the detector also has less than 100% fill factor, the nomogram must be modified accordingly. Both these parameters cause a global attenuation of both background and signal, corresponding to a left shift of the top horizontal red axis (as a large sensor with attenuation can be considered equivalent to a smaller sensor with 100% efficiency). For example, point "B" in Figure 19 represent 100% detection efficiency, no optical loss, 100% target reflectance, 24 μm detector side (in order to limit to 10^{10} ph/s the background rate). With realistic specification, such as 70% detection efficiency, 80% optical efficiency, 70% target reflectance, and still assuming 10^{10} ph/s background on the detector, the sensor size should be 38 μm, i.e. equal to a sensitive area increase of $1/(0.7 \times 0.8 \times 0.7)$.

A. Number of Repetitions for SPADs

In the previous nomogram, we considered 1000 acquisitions to collect the time-of-flight histogram for SPAD and digital SiPM detectors. In order to describe the relationship between number of repetitions and success ratio, we created the nomogram in Figure 20, where the vertical axis is the cumulated number of impinging signal photons after all acquisitions. A low repetition number causes the SPAD to detect just few photons, failing if background increases just above 1 Mcps; conversely, a higher repetition number causes an increased minimum signal intensity to be required, but allows operation even with higher background due to a better statistic in the histogram. For the same amount of impinging photons across n acquisitions, the SPAD sensitivity is spoiled when n is increased at constant background.

This can be seen in Figure 20, where one photon is enough at very low background for less than 10 repetitions, while 4 photons are needed up to about 1000 repetitions, and 6 photons at least are required for more than 10,000 repetitions.

For example, with 10^4 arrival signal photons, the maximum background is about $2{\cdot}10^6$ ph/s when just one laser shot is used; instead, using 100 repetitions allows for a stronger background in the order of 10^7 ph/s, whereas with 1000 repetitions the maximum background is increased up to almost $3{\cdot}10^7$ ph/s.

B. Number of Cells for an Analog SiPM

For both analog and digital SiPMs, changing the number of microcells (at same total area) strongly impacts operating

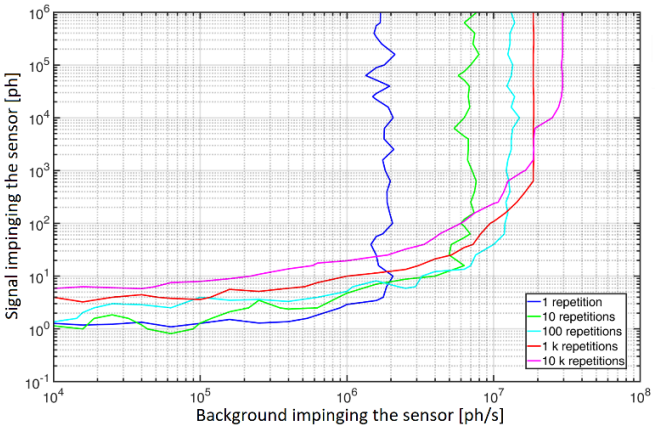

Fig. 20. Nomogram for a SPAD detector, at different number of repetitions required to collect the TOF histogram. Values on the Y axis represent the cumulative number of photons impinging to the sensor.

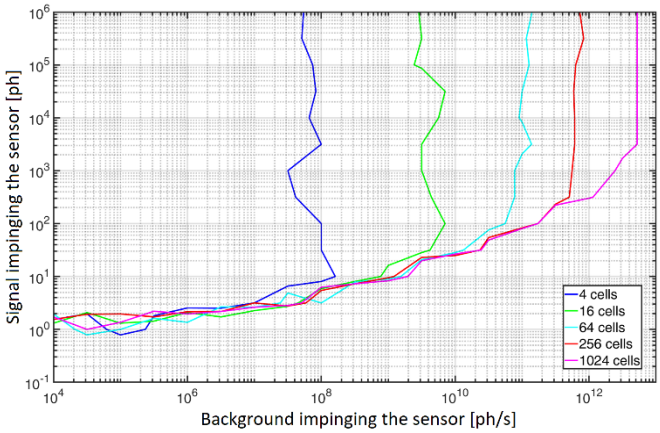

Fig. 21. Nomogram for a SiPM detector, at different number of microcells. Values on the Y axis represent the number of photons impinging to the sensor.

conditions. Higher number of microcells allows to operate the analog SiPM with stronger background, thus theoretically reaching APD performance, while losing the capability of detecting one single-photon because of limited dynamic range, e.g. with 1024 cells and an output dynamic range of 3 V each single photon event will be less than 3 mV high, so a single photon event can be covered by the electronic noise.

Figure 21 shows the nomogram trend for an analog SiPM with increasing number of microcells, without considering that the maximum density of microcells is actually dictated by physical constraints. Figure 19 can be used to have a reference between the sensor size and the background photon rate; using the same optical parameters as in paragraph V we can associate to 10^4 ph/s a size of 24 nm and so on for the other backgrounds.

C. Number of Concurrent Photons for a Digital SiPM

For a digital SiPM, an increased number of microcells does not directly lead to a higher success ratio at high background, as the sensor performance is also limited by SPAD dead-time and the photon threshold. In order to reach good performance with both low and high background levels, a variable threshold

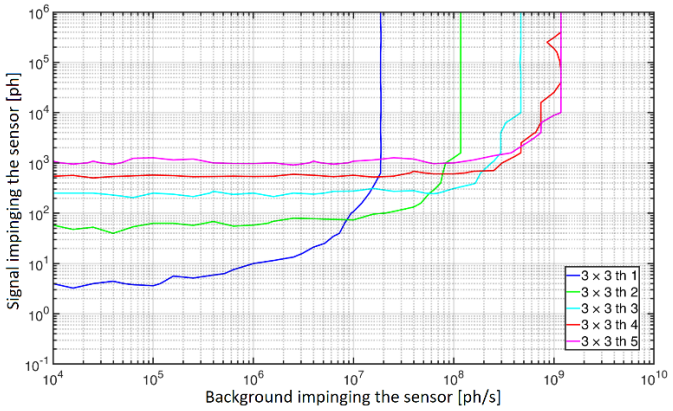

Fig. 22. Nomogram for a digital SiPM when changing the threshold of the minimum number of concurrent photons that may trigger a TDC conversion. Values on the Y axis represent the cumulative number of photons impinging to the sensor.

on the number of concurrent photons, i.e. triggered microcells, is mandatory. Figure 22 shows the effect of changing such a threshold for a given number of microcells in the digital SiPM, having fixed the repetition number to 1000. As can be seen, an increase in threshold allows the sensor to better sustain high background but worsens its sensitivity at low signal levels. For example, with threshold set to one photon, single-photon sensitivity is achieved at the expense of a low maximum allowed background (about $2{\cdot}10^7$ ph/s); instead, if the threshold is increased for instance to two photons, high background flux capability is improved (up to 10^8 ph/s) at the expense of a worse sensitivity, forcing an increase in the emitted signal power.

When the threshold is higher than one photon, the possibility to rearm the SPAD to detect more than just one photon in each laser repetition assumes an important role, as it gives the possibility to effectively reject early background photons by rearming each SPAD (20 ns of holdoff time) if the photon threshold is not reached. For instance, in a pixel composed by 4 SPADs and threshold equal to 3 photons, if two SPADs get triggered by early background photons there is no possibility to detect a signal event, unless the capability to rearm each SPAD after a photon detection is implemented.

The saturation shown in Figure 22 is due to both the holdoff time and to the number of cells. The reduction of holdoff can be very challenging, but will shift the saturation toward the right. Therefore, increasing the number of cells with the same area can be "easier" and theoretically can shift the saturation to the right. Note that a different number of cells for the same threshold value gives different results.

VI. Conclusions

Our work aimed at defining a nomogram allowing end-users to select the most suitable detector for the desired time-of-flight based LiDAR application, given laser energy budget, background ambient light, and technology limitations (e.g. detector performance). To this purpose, we compared the performance achievable by four different sensor topologies (namely APDs, SPADs analog SiPMs and digital SiPMs), operated either in analog or digital mode, capable of detecting single-photons or even resolve the number of photodetections, in presence of strong ambient background. To perform a fair comparison, we implemented Matlab simulations for each detector and we compared them with experimental acquisitions. Once validated, we employed the modelling to construct a nomogram able to give information about the best-suited detector in the desired operating condition.

From these results, we discussed how the SPAD single-photon sensitivity is impaired by its count-rate limitations and pile-up effect, and how to trade-off between sensor size and laser pulse energy. Conversely, APDs can be used with high background intensities, if large enough sensors are exploited, but their integration into large arrays may be problematic.

Eventually, provided that a sufficiently high number of microcells is available, SiPMs may be suitable for high background applications as they sit between SPADs and APDs performance both at very low signal intensities (if the background light is sufficiently weak) and at high background levels without saturation (even though they would require higher laser energy compared to APDs).

References

[1] A. Abosekeen, A. Noureldin, and M. J. Korenberg, "Utilizing the ACC-FMCW radar for land vehicles navigation," in *Proc. IEEE/ION Position, Location Navigat. Symp. (PLANS)*, Monterey, CA, USA, Apr. 2018, pp. 124–132.

[2] D. Gavrila and J. Giebel, "Shape-based pedestrian detection and tracking," in *Proc. Intell. Vehicle Symp.*, Versailles, France, Jun. 2002, pp. 8–14.

[3] R. Lussana, F. Villa, A. D. Mora, D. Contini, A. Tosi, and F. Zappa, "Enhanced single-photon time-of-flight 3D ranging," *Opt. Express*, vol. 23, no. 19, pp. 24962–24973, Sep. 2015.

[4] A. McCarthy, R. J. Collins, N. J. Krichel, V. Fernández, A. M. Wallace, and G. S. Buller, "Long-range time-of-flight scanning sensor based on high-speed time-correlated single-photon counting," *Appl. Opt.*, vol. 48, no. 32, pp. 6241–6251, Nov. 2009.

[5] R. Halterman and M. Bruch, "Velodyne HDL-64E lidar for unmanned surface vehicle obstacle detection," *Proc. SPIE*, vol. 7692, May 2010, Art. no. 76920D.

[6] F. Villa *et al.*, "CMOS imager with 1024 SPADs and TDCs for single-photon timing and 3-D time-of-flight," *IEEE J. Sel. Topics Quantum Electron.*, vol. 20, no. 6, pp. 364–373, Nov. 2014.

[7] C. Niclass, A. Rochas, P.-A. Besse, and E. Charbon, "Design and characterization of a CMOS 3-D image sensor based on single photon avalanche diodes," *IEEE J. Solid-State Circuits*, vol. 40, no. 9, pp. 1847–1854, Sep. 2005.

[8] F. Zappa, S. Tisa, A. Tosi, and S. Cova, "Principles and features of single-photon avalanche diode arrays," *Sens. Actuators A, Phys.*, vol. 140, no. 1, pp. 103–112, Oct. 2007.

[9] R. Lussana, "Time-of-flight CMOS single-photon cameras for high frame rate 2D imaging and 3D ranging, Chapter 5.2.3—iToF hold-off limitation," Ph.D. dissertation, DEIB, Politecnico di Milano, Milan, Italy, Feb. 2017, pp. 129–134.

[10] S. Tisa, F. Zappa, A. Tosi, and S. Cova, "Electronics for single photon avalanche diode arrays," *Sens. Actuators A, Phys.*, vol. 140, no. 1, pp. 113–122, Oct. 2007.

[11] K. F. Li *et al.*, "Avalanche multiplication noise characteristics in thin GaAs p^+-i-n^+ diodes," *IEEE Trans. Electron Devices*, vol. 45, no. 10, pp. 2102–2107, Oct. 1998.

[12] K. Yamamoto, K. Yamamura, K. Sato, T. Ota, H. Suzuki, and S. Ohsuka, "Development of multi-pixel photon counter (MPPC)," in *Proc. IEEE Nucl. Sci. Symp. Conf. Rec.*, 2006, pp. 1094–1097.

[13] S. L. Vinogradov, "Evaluation of performance of silicon photomultipliers in lidar applications," *Proc. SPIE*, vol. 10229, May 2017, Art. no. 102290L.

[14] R. Lange, "3D time-of-flight distance measurement with custom solid-state image sensors in CMOS/CCD-technology," Siegen Univ., Siegen, Germany, Tech. Rep. URN 467-1783, 2000, pp. 85–97. [Online]. Available: https://dspace.ub.uni-siegen.de/handle/ubsi/178

[15] C. A. Gueymard, D. Myers, and K. Emery, "Proposed reference irradiance spectra for solar energy systems testing," *Sol. Energy*, vol. 73, no. 6, pp. 443–467, Dec. 2002.
[16] M. G. Bulmer, *Principles of Statistics*. Mineola, NY, USA: Dover, 1979.
[17] D. Bronzi, S. Tisa, F. Villa, S. Bellisai, A. Tosi, and F. Zappa, "Fast sensing and quenching of CMOS SPADs for minimal afterpulsing effects," *IEEE Photon. Technol. Lett.*, vol. 25, no. 8, pp. 776–779, Apr. 15, 2013.
[18] P. A. Hiskett *et al.*, "Performance and design of InGaAs/InP photodiodes for single-photon counting at 155 μm," *Appl. Opt.*, vol. 39, no. 36, p. 6818, Dec. 2000.
[19] W. Becker, *The Becker&Hickl TCSPC Handbook*, 8th ed. Berlin, Germany, 2019. [Online]. Available: https://www.becker-hickl.com/
[20] M. Ghioni, S. Cova, F. Zappa, and C. Samori, "Compact active quenching circuit for fast photon counting with avalanche photodiodes," *Rev. Sci. Instrum.*, vol. 67, no. 10, pp. 3440–3448, Oct. 1996.
[21] F. Villa, Y. Zou, A. Dalla Mora, A. Tosi, and F. Zappa, "SPICE electrical models and simulations of silicon photomultipliers," *IEEE Trans. Nucl. Sci.*, vol. 62, no. 5, pp. 1950–1960, Oct. 2015.
[22] D. Portaluppi, E. Conca, and F. Villa, "32×32 CMOS SPAD imager for gated imaging, photon timing, and photon coincidence," *IEEE J. Sel. Topics Quantum Electron.*, vol. 24, no. 2, Mar. 2018, Art. no. 3800706.
[23] M. Beer, J. Haase, J. Ruskowski, and R. Kokozinski, "Background light rejection in SPAD-based LiDAR sensors by adaptive photon coincidence detection," *Sensors*, vol. 18, no. 12, p. 4338, Dec. 2018.
[24] Excelitas. *Silicon Avalanche Photodiode (APDs) for LiDAR—C30737*. [Online]. Available: http://www.excelitas.com/Downloads/DTS_C30737PH.pdf
[25] Hamamatsu. *MPPC (Multi-Pixel Photon Counter)—S13360*. [Online]. Available: https://www.hamamatsu.com/resources/pdf/ssd/s13360_series_kapd1052e.pdf
[26] S. Jagannathan *et al.*, "Efficient object detection and classification on low power embedded systems," in *Proc. IEEE Int. Conf. Consum. Electron. (ICCE)*, Las Vegas, NV, USA, Jan. 2017, pp. 233–234.

Klaus Pasquinelli was born in Seriate, Italy, in 1994. He received the bachelor's and M.Sc. degrees in electronics engineering from Politecnico di Milano in 2016 and October 2018, respectively, where he is currently pursuing the Ph.D. degree in information technology. His research interests include the design, development, and testing of systems with single-photon avalanche diodes' (SPADs) matrices and digital silicon photomultiplier (dSiPM).

Rudi Lussana was born in Bergamo, Italy, in 1989. He received the bachelor's degree, the M.Sc. degree in electronics engineering, and the Ph.D. degree in information technology from Politecnico di Milano in 2011, 2013, and 2017, respectively. He has been working towards the development of single-photon cameras, based on arrays of SPADs, for time-correlated single-photon counting applications.

Simone Tisa was born in Milano, Italy, in 1977. He received the M.Sc. *(summa cum laude)* degree in electronics engineering and the Ph.D. degree in electronics from Politecnico di Milano in 2001 and 2006, respectively. His research interests are connected with the use of single-photon detectors and active-quenching circuits for ultra-fast imaging applications in astrophysics, and with the design of bidimensional arrays of single-photon avalanche diodes with integrated electronics for the acquisition of time resolved images at single-photon level.

Federica Villa (Member, IEEE) was born in Milano, Italy, in 1986. She received the B.Sc. degree in biomedical engineering, the M.Sc. *(summa cum laude)* degree in electronic engineering, and the Ph.D. degree in information and communication technology from Politecnico di Milano in 2008, 2010, and 2014, respectively. She has been an Assistant Professor with Politecnico di Milano since 2015. She is the coauthor of about 100 articles. Her present research activities include the design and development of CMOS SPAD imagers for 2-D imaging via single-photon counting and 3-D ranging through direct time-of-flight photon-timing.

Franco Zappa (Senior Member, IEEE) was born in Milano, Italy, in 1965. He received the master's degree in electronics engineering and the Ph.D. degree in communication technology from Politecnico di Milano in 1989 and 1993, respectively. He has been a Full Professor of Electronics with Politecnico di Milano since 2011. In 2004, he cofounded Micro Photon Devices focused on the production of SPAD modules and cameras for single photon-counting and photon-timing. He is the coauthor of more than 250 articles published in peer-reviewed journals and conference proceedings, and eight text books on electronic design, electronic systems, and microcontrollers. His research interests include microelectronic circuitry for single-photon detectors (SPAD) and CMOS and BCD SPAD imagers, for high-sensitivity time-resolved optical measurements, 2-D imaging, and 3-D depth ranging via single-photons' time-of-flight.